Visualizing strongly-correlated electrons with a novel scanning tunneling microscope

Battisti, I.

4

Universality of pseudogap and emergent order in lightly doped Mott insulators

This chapter has been published as:
Battisti *et al.*, Nat. Phys. **13**, 21 (2017).

4.1 Introduction

Mott insulators are one of the most iconic examples of correlated electron systems. In these materials, electrons are localized due to strong electron-electron interactions, and they can be thought of as frozen at the location of their atomic core (see Sec. 1.2). A core mystery of condensed-matter physics is how this rigid arrangement of electrons loosens when inserting extra carriers (doping). The strong electron correlations that characterize the Mott insulating state, in fact, are thought to be responsible for the remarkably complex, emerging behaviors that are observed upon doping [6, 9, 11].

A prime example are cuprates, copper-oxide based compounds (see Sec. 1.2 for a brief overview). Upon adding extra carriers to the Mott insulating parent compound, cuprates show, at low doping levels, the formation of a pseudogap and a variety of inhomogeneous electronic orders, and, at higher doping, high-T_c superconductivity [11]. These phenomena have often been assumed (though not verified), to not be limited to the CuO_2 planes, but common to spin-$\frac{1}{2}$ Mott physics.

Here, we study the iridate Sr_2IrO_4, a compound that is chemically radically different from cuprates, but also an effective spin-$\frac{1}{2}$ quasi two-dimensional Mott insulator. We show that, upon electron doping, a spatially inhomogeneous pseudogap as well as a local glassy charge order exists in this compound as well, revealing an universality of these emergent phenomena. Moreover, we are able to precisely elucidate how the insertion of extra carriers causes the transition from Mott to pseudogap phase.

We start with an introduction to the properties of Sr_2IrO_4 and an overview of the relevant literature (Sec. 4.2 and 4.3). We then show our STM results on the electron-doped compound $(Sr_{1-x}La_x)_2IrO_4$, at doping levels $0 \leq x \leq 5.5\,\%$. We find two distinct electronic behaviors, one at low doping levels, $x \leq 4\%$ (Sec. 4.5), and one at higher doping levels, $x \approx 5\%$ (Sec. 4.6). In section 4.7, we illustrate the melting of the Mott state with doping, and we propose a theoretical interpretation of our data.

4.2 The electron-doped iridate $(Sr_{1-x}La_x)_2IrO_4$

The parent compound Sr_2IrO_4 is a quasi two-dimensional material, isostructural to the cuprate La_2CuO_4. It has a perovskite crystal structure with alternating IrO_2 and SrO planes, such that oxygen octahedra form around each iridium atom. The IrO_6 octahedra additionally undergo an in-plane rotation of 11° (Fig. 4.1a).

Each iridium atom has five $5d$ electrons ($5d^5$), in contrast to the cuprates, where each copper atom has nine $3d$ electrons ($3d^9$). As introduced in chapter 1, the orbitals of $5d$ transition metal atoms are more spatially extended than those of $3d$ transition metals, causing larger bandwidths and higher hopping energy t. Moreover, the

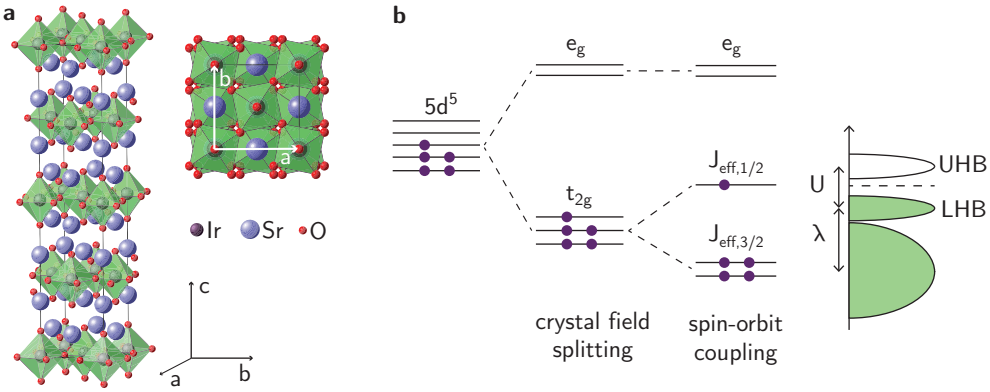

Figure 4.1: **a**, Crystal structure of Sr_2IrO_4. **b**, Effect of crystal field and spin-orbit coupling on the 5d band of Sr_2IrO_4. The Coulomb repulsion U splits the resulting $J_{eff} = 1/2$ band into a lower and upper Hubbard band (LHB and UHB, respectively) [71].

electron-electron correlations caused by the Coulomb repulsion U are reduced due to higher screening compared to $3d$ elements (for $3d$ materials the electron correlation magnitude is $U \approx 5\,\text{eV}$, for $5d$ materials typically $U \approx 0.5\,\text{eV}$). Despite the weaker electron-electron correlation U which is not able to open a Mott gap in the spatially extended $5d$ states, Sr_2IrO_4 is found to be an effective spin-$\frac{1}{2}$ Mott insulator [71, 72]. This can be explained by the fact that $5d$ atoms are heavier and therefore have a stronger spin-orbit coupling: while in cuprates spin-orbit coupling is typically negligible, in the iridates it acquires energies comparable to the electron-electron correlations.

Fig. 4.1b illustrates how this affects the electronic structure. The $5d$ states are first split by the crystal field into three t_{2g} states and two e_g states, analogous to cuprates. The crystal field energy is large enough that the five electrons prefer a low spin state and occupy only the t_{2g} states. At this point, the moderate electron correlations U are not able to open a Mott gap within the t_{2g} band. However, the strong spin-orbit coupling splits the t_{2g} band to form a filled $J_{eff} = \frac{3}{2}$ band and a half-filled $J_{eff} = \frac{1}{2}$ band. The moderate on-site Coulomb repulsion U is now strong enough to open a Mott gap in the $J_{eff} = \frac{1}{2}$ band, making Sr_2IrO_4 an effective spin-$\frac{1}{2}$ Mott insulator [71, 72].

Theoretical calculations, including LDA[1]+SO+U [71, 73], variational Monte Carlo studies [74] and LDA+DMFT[2] [75] confirm this scenario.

Experimentally, the parent compound Sr_2IrO_4 has been probed by several techniques. Optical conductivity measurements [71, 73, 76] show a Mott gap value of $\approx 500\,\text{meV}$,

[1] LDA: local-density approximation.
[2] DMFT: dynamical mean-field theory.

in good agreement with calculations [77]. Angle-resolved photoemission spectroscopy (ARPES) shows that the Mott gap is asymmetric around the Fermi level, with the upper edge of the lower Hubbard band between -200 meV and -100 meV [71, 78–80]. Resonant (inelastic) x-ray scattering (REXS - RIXS) shows antiferromagnetic ordering typical of the Mott state, with the magnetic moments $J_{eff} = \frac{1}{2}$ lying in the IrO_2 plane, and additionally canted due to the rotation of the ochtaedra [81]. The spin excitations as measured with RIXS have energies comparable to the ones of the cuprates [82], and REXS data has revealed the presence of an incommensurate magnetic state reminiscent of the diagonal spin density wave state observed in the cuprate $(La_{1-x}Sr_x)_2CuO_4$ [83].

Given the insulating behavior of the material at low temperatures, pioneering STM measurements are reported for the parent compound only at 77 K [84–86], each of them showing different Mott gap values. Accidental doping was reported in one study [84], indicating a possible cause of the different values.

Despite the very different chemical make-up, the similarity of Sr_2IrO_4 to the parent compound of cuprate superconductors is striking. It thus seems straightforward to expect that doping the material with holes or electrons will display the same mysterious phases that emerge upon doping cuprates. Indeed, theoretical studies predict that the material should become superconducting upon electron doping [87, 88].

Electron-doped samples have been created by depleting oxygen [89] or substituting La at the Sr sites in bulk crystals [79, 80, 90–92] and by surface doping through *in situ* deposition of alkali-metal atoms [93, 94]. Hole-doped samples have been made by substituting Rh at the Ir sites [80, 90]. In all cases, doping quickly suppresses magnetism and affects transport results. Moreover, there is consensus about the appearance of a pseudogap [79, 92, 93] and of a low-temperature *d*-wave gap [94, 95] upon electron doping. Unfortunately, superconductivity has not been achieved to date, possibly because samples with sufficiently high doping levels could not be created.

4.3 Sample characterization

We think that the most reliable way to dope Sr_2IrO_4 with extra electrons is by La substitution on the Sr sites, because this method produces the cleanest crystals. Therefore, the results presented in this chapter are measured on single crystal $(Sr_{1-x}La_x)_2IrO_4$ samples, spanning the doping range $0 \leq x \leq 5.5\,\%$. The samples are grown and pre-characterized by our collaborators from University College London and University of Geneva, who performed ARPES experiments on samples from the same batch [79]. The single crystals are flux grown from a mixture of off-stoichiometric quantities of IrO_2, La_2O_3 and $SrCO_3$ in an anhydrous $SrCl_2$ flux. The mixture is

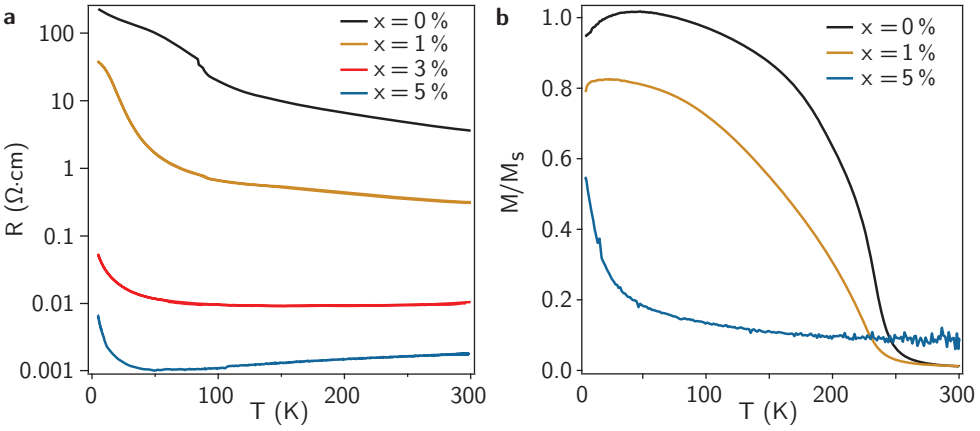

Figure 4.2: **a**, Evolution of the resistivity with doping. **b**, Evolution of the magnetic behavior with doping. The magnetization curves are taken with an applied magnetic field of $H = 1\,T$ after zero-field cooling and are normalized by the magnetic moment at $H = 2\,T$, which for the magnetic samples corresponds to the saturation field. Reproduced from Ref. [79].

heated to 1245 °C for 12 h and cooled at a rate of $8\,°C\,h^{-1}$ to 1100 °C before quenching to room temperature. The resulting crystals are mechanically separated from the flux by washing with water, and range between 200 µm and 600 µm in size.

Transport measurements of the *ab*-plane resistivity at different doping concentrations x (as determined by EDX[3]) are shown in Fig. 4.2a. For the highest doping level, the resistivity shows metallic behavior down to 50 K followed by an upturn at lower temperature. The upturn is reported from several groups [80, 91, 92, 96], and is reminiscent of low-doped cuprates [97]. Figure 4.2b shows the doping evolution of the magnetic behavior. The magnetic order persists for $x = 1\%$, but with decreased Neel temperature; the highest doping samples are paramagnetic, indicating suppression of the Mott antiferromagnetic state.

These bulk transport measurements probe the properties of the material between two macroscopically spaced electrodes (in this case, applied on two sides of the crystal). If the material is electronically inhomogeneous, transport will average the electronic properties and the interpretation of its results becomes more complicated. Importantly, we know from our STM measurements and from subsequent near-field optical microscopy measurements [96] that the doping concentration is not homogeneous within one $(Sr_{1-x}La_x)_2IrO_4$ sample. In samples with doping $x = 5\%$ determined by EDX, we find with STM areas where the local doping changes from $x = 2\%$ to $x = 5\%$ on a length-scale of $\approx 100\,\mu m$. In order to obtain more reliable results with easier interpretation, one should measure transport from areas where the doping is

[3] energy dispersive X-ray spectroscopy.

homogeneous, for example by using electron-beam lithography or focused-ion beam (FIB) to reduce the size of the crystals before measuring transport.

4.4 Doping level determination with STM

The STM experiments reported in this chapter are performed with a low-temperature (2 K), ultrahigh vacuum commercial STM[4]. The iridate crystals are cleaved *in situ* at a temperature of 20 K and a pressure of 2×10^{-10} mbar, and then transferred immediately into the STM sample stage. Importantly, we found that cleaving at a higher temperature deteriorates the quality of the surface. The STM topographs are taken in the constant current mode, and the $\mathrm{d}I/\mathrm{d}V$ spectra are collected using a standard lock-in technique with a modulation frequency of 857 Hz. We use mechanically ground PtIr tips that are tested on a crystalline Au(111) surface prepared *in situ* by Ar ion sputtering and temperature annealing.

The iridate $(Sr_{1-x}La_x)_2IrO_4$ cleaves between the SrO layers, revealing an atomically flat SrO terminated surface. In Fig. 4.3, we show two topographs at different doping concentrations. The Sr atoms are easily resolved, and the lattice constant is $a_0 = 3.9$ Å. Since La dopants substitute for Sr atoms, they are visible on the surface, and they can be identified as dark atoms surrounded by a brighter square [98].

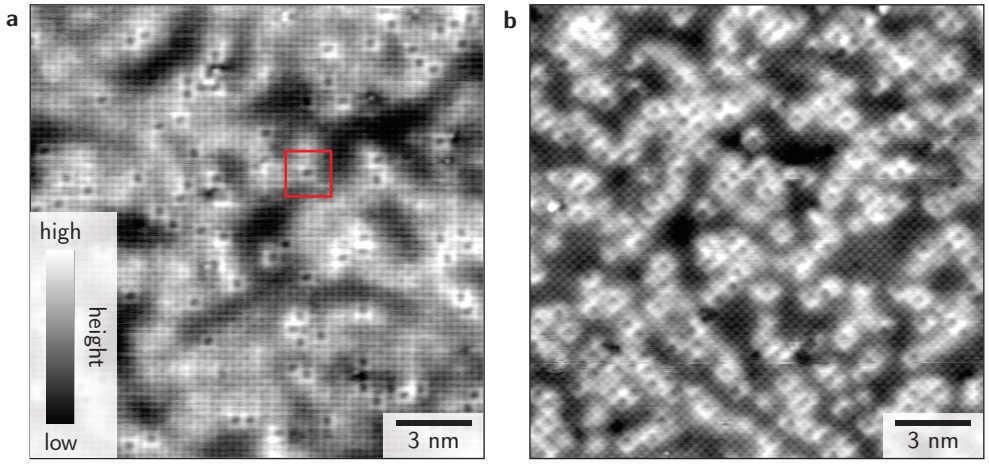

Figure 4.3: Examples of atomically resolved STM topographs measured on $(Sr_{1-x}La_x)_2IrO_4$ at different doping levels. The La^{3+} dopant atoms are readily identified as dark spots surrounded by brighter atoms (see, e.g., red square). **a**, Doping level 2.0%, field of view $18\times18\,\mathrm{nm}^2$, setup conditions ($V_b = -1.1$ V, $I_t = -200$ pA). **b**, Doping level 5.5%, field of view $18\times18\,\mathrm{nm}^2$, setup conditions ($V_b = -750$ mV, $I_t = -400$ pA).

[4]modified USM1500 from Unisoku.

The ability to easily identify the dopant positions with atomic precision (e.g. in contrast to the cuprates [17, 99]) is key to our investigation, as it allows us to precisely localize dopant atoms and investigate their effect on the electronic structure. As the doping inhomogeneities are large (see Sec. 4.3), it is important to determine the local doping level: with STM, we can simply do that by counting the La to Sr ratio within a given field of view.

We investigate surfaces with densely spaced local doping concentrations between 2.1 % and 5.5 %, where we estimate an error of ±0.7 % in the doping determination. We also attempt to measure an undoped sample, but even at 77 K the material is too insulating to allow STM experiments, and the tip crashes on the sample during the approach procedure. This is in contrast with previous measurements on the parent compound [84–86], which we interpret as a confirmation of the high purity of our samples.

In the available doping range, we find strikingly different spectroscopic properties that allow us to separate the doping levels into two main groups, one of *low doping*, where $x < 4\%$, and one of *high doping*, where $x \approx 5\%$.

4.5 Low doping levels: frozen Mott state

We find that very lightly doped samples with $x < 4\,\%$ are deep in the Mott phase. In all our measurements, these doping levels yield a clear Mott gap, as shown in Fig. 4.4 for a sample with $x = 2.2\,\%$. The shape of the gap is reminiscent of STM spectra of cuprate parent materials [100, 101].

To investigate how the Mott state reacts when dopant atoms are inserted, we acquire spectroscopic maps from which we extract Mott gap maps, i.e., the magnitude of the Mott gap as a function of location, $\Delta_{\mathrm{Mott}}(\mathbf{r})$. Figure 4.4a shows the result on a 2.2 % sample, where the La dopant positions are marked by green dots. The gap size is determined by fitting a phenomenological gap function consisting of two artificially broadened Fermi functions that have the gap energy as fitting parameter. We fit negative and positive sides separately.

The biggest variation in the Mott gap is highlighted in the inset of Fig. 4.4a, where the two spectra correspond to the average of all the spectra inside the white circles. The main difference is the small additional density of states around −0.8 eV. Importantly, La dopants do not significantly change the Mott gap size in their close vicinity. However, a long-wavelength arrangement of varying Mott gap is visible, and it is possibly induced by the presence of the dopants. We interpret these nanoscale arrangements as the first of a series of orders that will appear upon doping. The most surprising

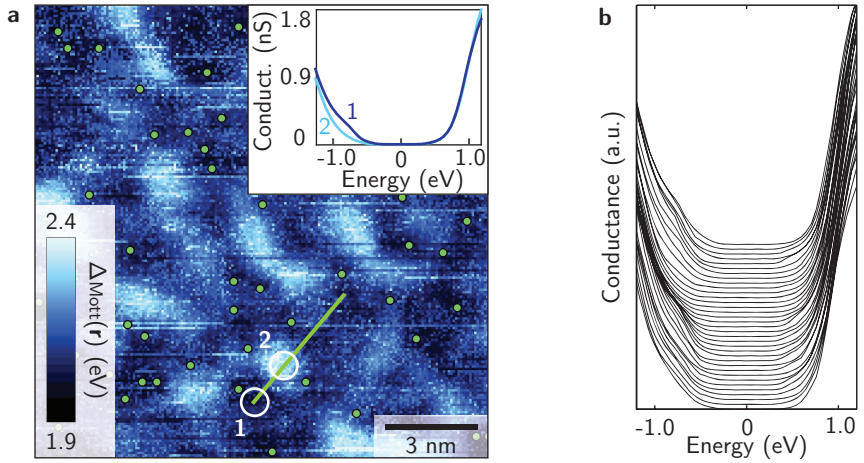

Figure 4.4: **a**, Mott gap map Δ_{Mott} of a sample with doping concentration $x = 2.2\,\%$. Position of dopant atoms are indicated by green circles. The inset shows local density of states spectra averaged inside the white circles. **b**, Local density of states spectra, each corresponding to a single measurement, along the green line in **a**, vertically offset for visual clarity.

observation is the total lack of in-gap states, despite the presence of dopants. We will discuss our interpretation of this fact in Sec. 4.7.

Another important observation regards the size of the gap: the magnitude of the Mott gap that we measure with STM on the lightly doped samples does not agree with what has been reported in literature by other techniques [71, 73, 77–79]. If we interpret the gap size as the energy range where the LDOS is zero, we measure a gap of $\approx 1\,\text{eV}$, which is very different from the 500 meV gap reported by optical spectroscopy and ARPES and predicted by theory [71, 73, 77–79].

This is caused by the phenomenon of tip-induced band bending (TIBB) that we introduced in Sec. 2.4. Due to the poor electronic screening in the material, the electric field generated by the tip can penetrate the sample, changing the potential landscape and strongly affecting the spectra measured with STM. In particular, TIBB can cause the gap measured with STM to be bigger than the intrinsic gap of the material.

In chapter 5, we show that this is exactly what happens in the lightly doped iridates, and we develop a model that is able to retrieve the intrinsic Mott gap from the apparent Mott gap measured by STM. Here, we just want to state that after applying our TIBB model to the data, we obtain an intrinsic gap value of $\approx 600\,\text{meV}$ for the low doping level samples, a value that roughly reconciles with literature.

4.6 High doping levels: pseudogap and electronic order

The pure Mott state described in section 4.5 is not sustained at higher doping levels $x \approx 5\%$. At this threshold, we find an abrupt transition to a strikingly inhomogeneous electronic structure, with a phase-separated Mott gap/pseudogap electronic landscape. Within the pseudogap regions, we additionally observe signatures of electronic order that are reminiscent of the order observed in the cuprates.

4.6.1 Phase separation

At doping levels of $x \approx 5\%$, the $\mathrm{d}I/\mathrm{d}V$ spectra drastically change[5]. In some regions we still measure a Mott gap, which now has the Fermi level pinned closer to the bottom of the upper Hubbard band (blue curve in Fig. 4.5a). This is in contrast to the low doping samples, and is to be expected for a Mott insulator doped with electrons. In other regions, we measure electronic states inside the Mott gap (red curve in Fig. 4.5a). Here, the spectra are remarkably similar to the pseudogap spectra in the cuprates [101, 102], with a gap value of 70 - 300 meV, in rough agreement with ARPES measurements [79, 93, 95]. In addition, some of the spectra show clear 'coherence peaks' (Fig. 4.5d).

In order to analyze how these two different types of spectra are spatially distributed within a field of view, we introduce a parameter that we call *Mott parameter*, $M(\mathbf{r})$. It is obtained by integrating the LDOS inside the Mott gap (red-shaded area in Fig 4.5b) and normalizing it by the integrated LDOS outside the gap (blue-shaded area in Fig 4.5b). In numbers,

$$M(\mathbf{r}) = \frac{\int_{-350\,\mathrm{meV}}^{+50\,\mathrm{meV}} \mathrm{LDOS}(E,\mathbf{r})\,\mathrm{d}E}{\int_{+200\,\mathrm{meV}}^{+500\,\mathrm{meV}} \mathrm{LDOS}(E,\mathbf{r})\,\mathrm{d}E}\,. \tag{4.1}$$

This parameter is large when there are states inside the gap, and small when the Mott gap is dominating. In Fig. 4.5c, we plot $M(\mathbf{r})$ as a function of the spatial coordinates for a spectroscopic map measured on a $x = 5.5\,\%$ surface, with the dopant atoms positions indicated by green dots. This allows us to quickly identify Mott areas (in blue) vs. pseudogap areas (in red).

The pseudogap areas, that we will, from now on, call *pseudogap puddles*, are not randomly distributed, but form around clusters of dopant atoms. We want to emphasize that pseudogap puddles are not observed in the low doping level samples, even if few dopants happen to be close together by chance: a certain threshold in the doping level is needed for the transition to occur. Moreover, the transition between the two

[5] This is also reported by Chen et al. [92].

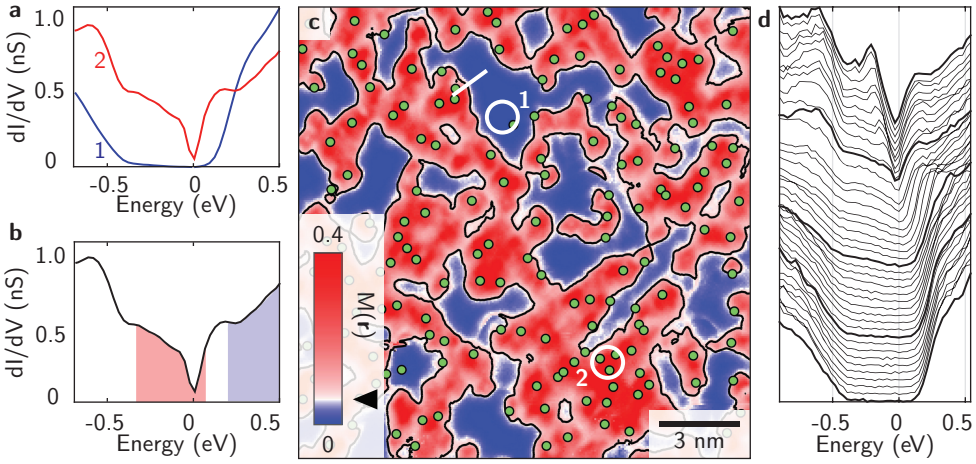

Figure 4.5: Phase separated Mott/pseudogap electronic structure at 5.5 % doping. **a**, Spectra from two different regions: Mott spectrum (blue), and mixed Mott/pseudogap spectrum (red). The spectra are the average of 180 spectra inside the white circles in panel **c**. **b**, Definition of the Mott parameter as the integrated LDOS inside the Mott gap (red) normalized by the one outside the gap (blue). **c**, The Mott parameter identifies pseudogap puddles (red) and pure Mott regions (blue). Green circles indicate the La dopant locations. The triangle on the colorbar indicates the value of the black contour. **d**, Local density of states spectra along the white line in **c** (whose length is 1.5 nm), vertically offset for clarity. Each spectrum corresponds to a single measurement.

regimes of different electronic behavior is well defined and sharp, in the sense that it occurs within less than a nanometer. We highlight the sharpness in Fig. 4.5d, where we show single spectra along the white line in Fig. 4.5c. This sharpness allows us to define a threshold between Mott and pseudogap regions (black contour in Fig. 4.5c), and to state that we observe an *electronic phase separation* at the nanoscales.

4.6.2 Mapping pseudogap and Mott gap

To further characterize the electronic structure, we develop a fitting procedure that is able to fit spectra both in the Mott regions and in the pseudogap puddles. We choose to use a largely phenomenological fitting function, given that the vast variety of the spectra complicates the development of a complete theory. It comprises a polynomial background that multiplies a phenomenological Mott gap summed with a phenomenological pseudogap (see Fig. 4.6a for a graphic representation):

$$\mathrm{LDOS}_{\mathrm{total}}(E) = \mathrm{LDOS}_{\mathrm{background}}(E) \cdot [\mathrm{LDOS}_{\mathrm{Mott}}(E) + \mathrm{LDOS}_{\mathrm{PG}}(E)]. \qquad (4.2)$$

The polynomial background density of states is given by

$$\mathrm{LDOS}_{\mathrm{background}}(E) = a\,E^2 + b, \tag{4.3}$$

where and a and b are fitting parameters. The phenomenological Mott gap Δ_{Mott} consists of two slightly broadened gap edges, asymmetric around the chemical potential:

$$\mathrm{LDOS}_{\mathrm{Mott}}(E) = \left| \frac{1}{1+e^{(-E-E_0)/w}} - \frac{1}{1+e^{(-E+E_0-\Delta_{\mathrm{Mott}})/w}} \right|, \tag{4.4}$$

where w gives the broadening, E_0 is the energy where the upper Hubbard band roughly pins to the chemical potential and Δ_{Mott} is the size of the Mott gap. We keep the first two parameters fixed ($w = 0.026\,\mathrm{eV}$, $E_0 = 0.1\,\mathrm{eV}$), while the size of the Mott gap is used as a fitting parameter. To fit the pseudogap, we follow ARPES results on electron-doped Sr_2IrO_4 [79, 95] and use a phenomenological function inspired by the d-wave gap function commonly used to fit cuprates spectra [103, 104]:

$$\mathrm{LDOS}_{\mathrm{PG}}(E) = C_0 \left| \frac{E + i\alpha\sqrt{E}}{\sqrt{\left(E + i\alpha\sqrt{E}\right)^2 - \Delta_{\mathrm{PG}}^2}} \right|. \tag{4.5}$$

It contains two fitting parameters: a scaling factor C_0 and the size of the pseudogap Δ_{PG}. We keep α, the effective scattering rate, fixed to $0.2\,\mathrm{eV}^{1/2}$. The square root in the imaginary part is selected to ensure a rather constant broadening independent of the gap.

All the spectra of the spectroscopic map shown in Fig. 4.5 are fitted with this function, using the least squares method. Since for this doping level the upper edge of the Mott gap is pinned to the chemical potential, and because in that location pseudogap and Mott gap overlap, we fit the model to the data only for negative energies. We are able to obtain excellent fits to all the spectra. This allows us to simultaneously extract both the pseudogap Δ_{PG} and the Mott gap Δ_{Mott} for all the spectra, and to plot them as a function of location, as it is shown in Fig. 4.6c-d. From these plots we can learn how the gaps are spatially distributed, and hence what are the length-scales at which the gap widths change. We can then additionally investigate the correlations between the two gaps for $> 10^4$ spectra located in the pseudogap puddles, as it is shown in Fig. 4.6b. We find a positive correlation of 0.31, i.e. the larger the Mott gap, the larger the pseudogap.

In general, the microscopic origin of the pseudogap in electron-doped Sr_2IrO_4 is still a matter of debate. Theoretical proposals include fluctuations of the long-range antiferromagnetic order [105] and the onset of short-range antiferromagnetic order [106]. The latter is supported by experimental evidence that the temperature at which the pseudogap opens ($\approx$100 K, from ARPES [93] and optical spectroscopy [76]) roughly

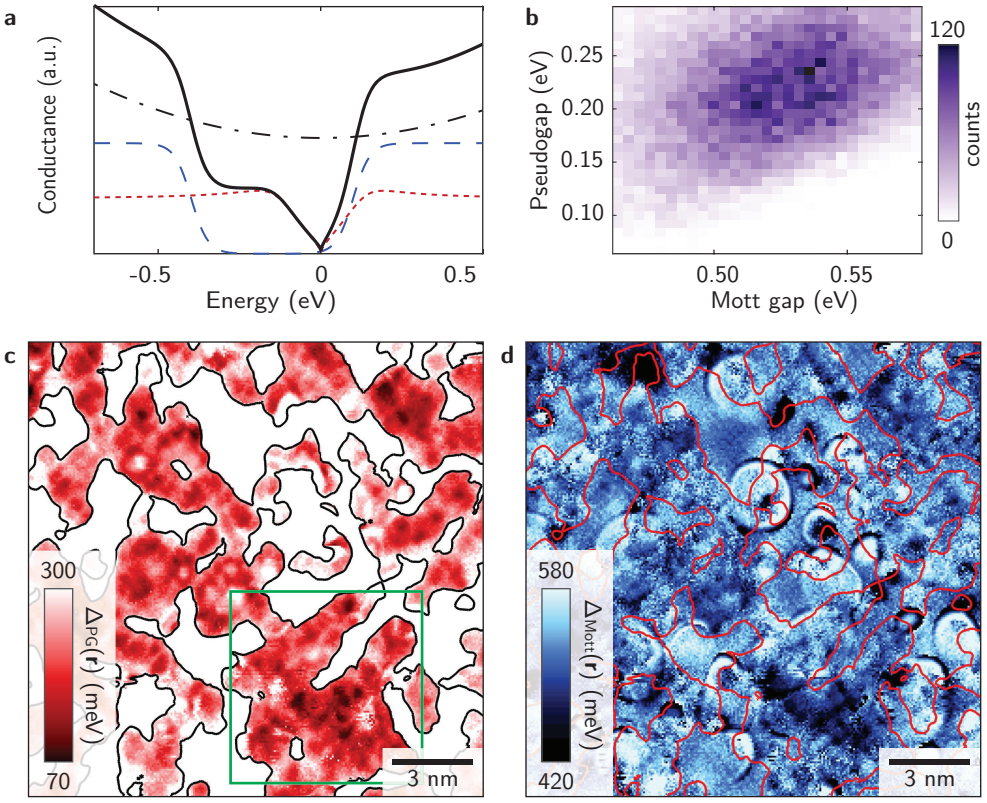

Figure 4.6: **a**, Phenomenological fit function to simultaneously extract both the Mott and pseudogap size. A parabolic density of states (dot-dashed, black) is multiplied with Mott gap (dashed, blue) summed with a V-shaped pseudogap (dotted, red). **b**, Correlation between Mott and pseudogap size for all the spectra showing a pseudogap in the field of view in panel **c**, plotted as a 2D-histogram where the colorscale indicates the amount of spectra falling in each bin. **c**, Pseudogap map extracted from the fitting procedure in the same field of view shown in Fig. 4.5. The green square indicates the area analyzed further in Fig. 4.7. **d**, Mott gap map simultaneously extracted from the same fitting procedure. The circular features are due to TIBB and will be discussed further in chapter 5.

coincides with the onset of short-range antiferromagnetic correlations measured with bulk magnetization and neutron scattering [92].

We interpret the positive correlation emerging from our data as evidence that pseudogap and Mott physics are intimately linked, therefore suggesting that the pseudogap might not simply be caused by magnetic correlations.

4.6.3 Emergent order

After observing the nucleation of pseudogap puddles in the samples, we want to test if the cuprate phenomenology can be extended further to this other lightly doped Mott insulator. In the low-doping region of the cuprates phase diagram, a sizable set of orders coexist, which are sometimes believed to cause the pseudogap [11]. In particular, these include disordered, stripy charge arrangements [4, 13, 19, 107, 108].

We therefore search for such ordered phases within the pseudogap puddles in our samples. We find that the spatial distribution of the pseudogap value, when extracted with atomic precision, reveals a striking tendency for order. We can observe in Fig. 4.6c and Fig. 4.7a that the Δ_{PG} gap maps exhibit glassy, locally unidirectional structures, reminiscent of lightly hole doped cuprates [4, 19, 103].

Glassy charge order is also visible in the density of states right outside the pseudogap. In Fig. 4.7c we show the conductance layer at $-210\,\mathrm{meV}$, where a stripy structure is clearly visible. When plotted together with the position of the Ir atoms (small green dots, while the big green dots still indicate the position of La dopants), it appears that the ordered arrangements consist of bond-centered, unidirectional objects of length scales of two to four Ir-Ir distances, clearly very disordered on a larger length scale. In Fig. 4.7d we show the laplacian of the ratio map $z = g(\text{-}210\,\mathrm{meV})/g(210\,\mathrm{meV})$ where the stripy order is emphasized. Similarly to the pseudogap, these arrangements also nucleate around the dopant atom positions and are not present in the Mott-like areas of the field of view.

The limited data that exist on underdoped cuprates [19, 101, 103] show that the patterns in the conductance layers get more disordered when patches of the sample become insulating. In our measurements, the pseudogap puddles are smaller than what has been observed on the cuprates, and we thus expect the disorder to be even stronger than in cuprates. In the last two panels of Fig. 4.7 we report examples from literature of how order manifests in the cuprates. In Fig. 4.7e, we show the conductance layer measured on an underdoped $Ca_{2\text{-}x}Na_xCuO_2Cl_2$ sample [103]. In Fig. 4.7f, we show the laplacian of the ratio map measured on a (DyBi)-2212 sample [19].

It is clear that the iridates are more disordered, with the stripy patterns appearing only in the pseudogap puddles, and becoming better arranged when the pseudogap puddles get bigger. We can therefore speculate that at higher doping the order observed in the iridates would resemble the one observed in the cuprates.

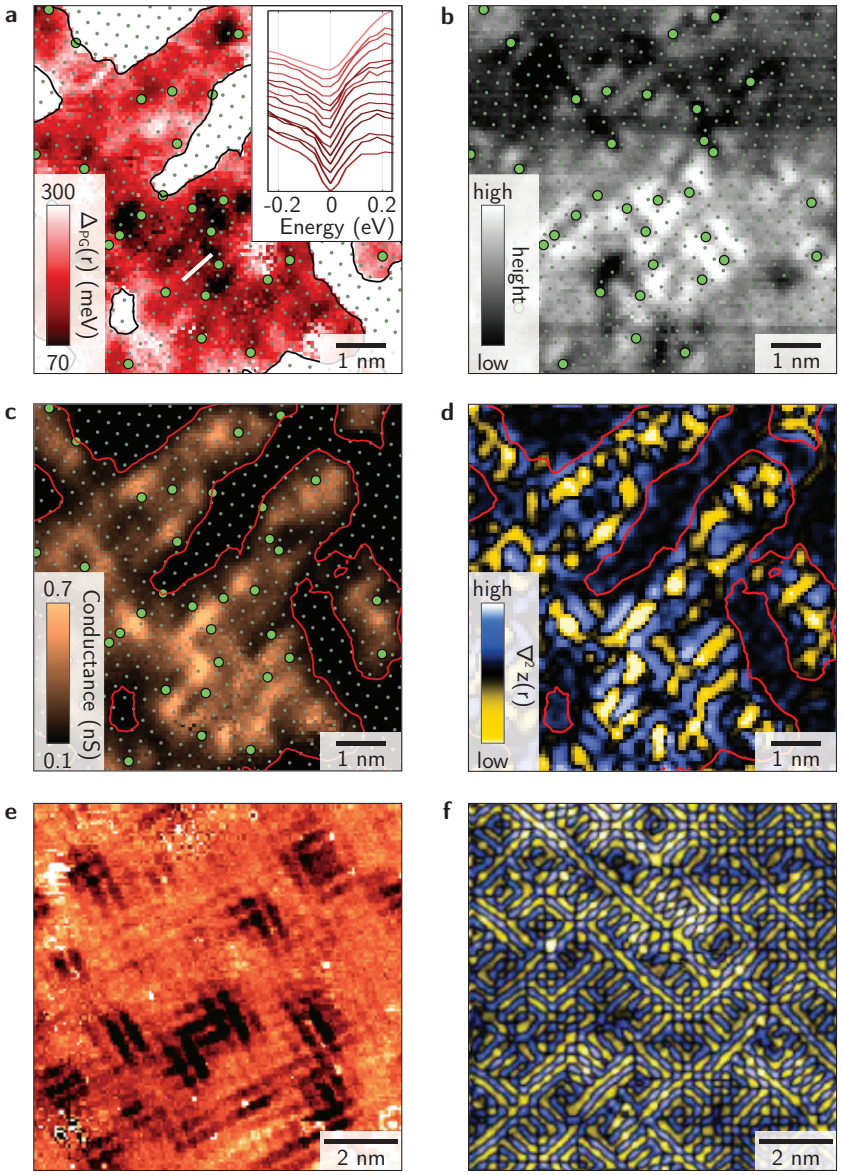

Figure 4.7: **a**, Map of the pseudogap Δ_{PG}, corresponding to the area in the green square from Fig.4.6c. The small green dots indicate Ir atom locations, the larger green circles indicate La dopant locations on the Sr sites. In the inset, spectra along the white line show the variations in the pseudogap, offset for clarity. **b**, Topograph in the same field of view, showing the atomic periodicity. **c**, Conductance layer $g = \mathrm{d}I/\mathrm{d}V$ at -210 meV. Glassy order is nucleating around the La dopant atoms. **d**, Laplacian of the ratio map layer $z = g(\text{-}210\,\text{meV})/g(210\,\text{meV})$. **e**, Conductance layer at -0.22 V measured on an underdoped $Ca_{2-x}Na_xCuO_2Cl_2$ sample, adapted from Ref. [103]. Glassy order is visible only whithin some areas. **f**, Laplacian of the ratio map $z = I(150\,\text{meV})/I(\text{-}150\,\text{meV})$ for a (Dy,Bi)-2212 sample, adapted from Ref. [19].

4.7 Doping evolution: a sharp transition

After illustrating the electronic behavior of the samples at low and high doping levels, we want to elucidate how the evolution towards the pseudogap phase occurs. Since in the iridate samples the dopant atoms can be seen on the surface, we have the unique possibility of measuring samples with densely-spaced local doping concentrations between $x = 2.1\,\%$ and $x = 5.5\,\%$. We measure spectroscopic maps with $> 10^6$ data-points at each doping concentration, and we analyze them using the methods described above. Figure 4.8 summarizes the results: Fig. 4.8a shows the evolution of the averaged spectra, Fig. 4.8b-g show the maps of the Mott parameter on the respective fields of view. For the measurements above $x = 4\,\%$, where phase separation is observed, we show the averaged spectra separately for the pseudogap regions (in red) and for the Mott regions (in blue).

It is clear that at a certain doping threshold, around $x = 5\,\%$, the electronic behavior undergoes an abrupt transition from a purely Mott-like state to a phase-separated Mott/pseudogap electronic landscape. At doping concentration below the transition threshold, none of the spectra exhibits any sort of impurity state, as we already emphasized in Sec. 4.5. Nor is the chemical potential pinned to the bottom of the upper Hubbard band, as one would expect from an electron-doped Mott insulator with shallow dopant centers. Moreover, the phenomenology of the electronic structure is surprisingly independent of the doping concentration for $x < 4\,\%$, showing a clear Mott gap with small variations. This leads to the question: Where did all the dopant electrons go?

We propose the scenario illustrated in Fig. 4.9. Randomly distributed La dopants form localized states within the forbidden energy gap, similarly to what happens when inserting donors in a semiconductor [109, 110]. At low doping, the dopant energy levels aggregate into a narrow range of energy, forming what in semiconductor parlance is called an 'impurity band' (note that this is a partially misleading term, as the electrons wave functions remain localized [110]). This nevertheless shifts the chemical potential to the mid-energy of the impurity band. In a simple one-electron picture and for shallow dopant centers, this scenario typically leads to a quick collapse of the insulating gap towards conductivity, with the impurity band merging into the conduction band and the chemical potential shifting into the latter. This simplified picture might however change when the extra electrons also experience the strong on-site Coulomb repulsion U. It was proposed by N.F. Mott that, due to the strong electron-electron correlations in the impurity band, a Mott gap can open in the latter, creating a filled lower band and an empty upper band [5, 110, 111].

We think that this is the scenario that can best explain our experimental results. There are however some points to address: How can we explain the total absence of

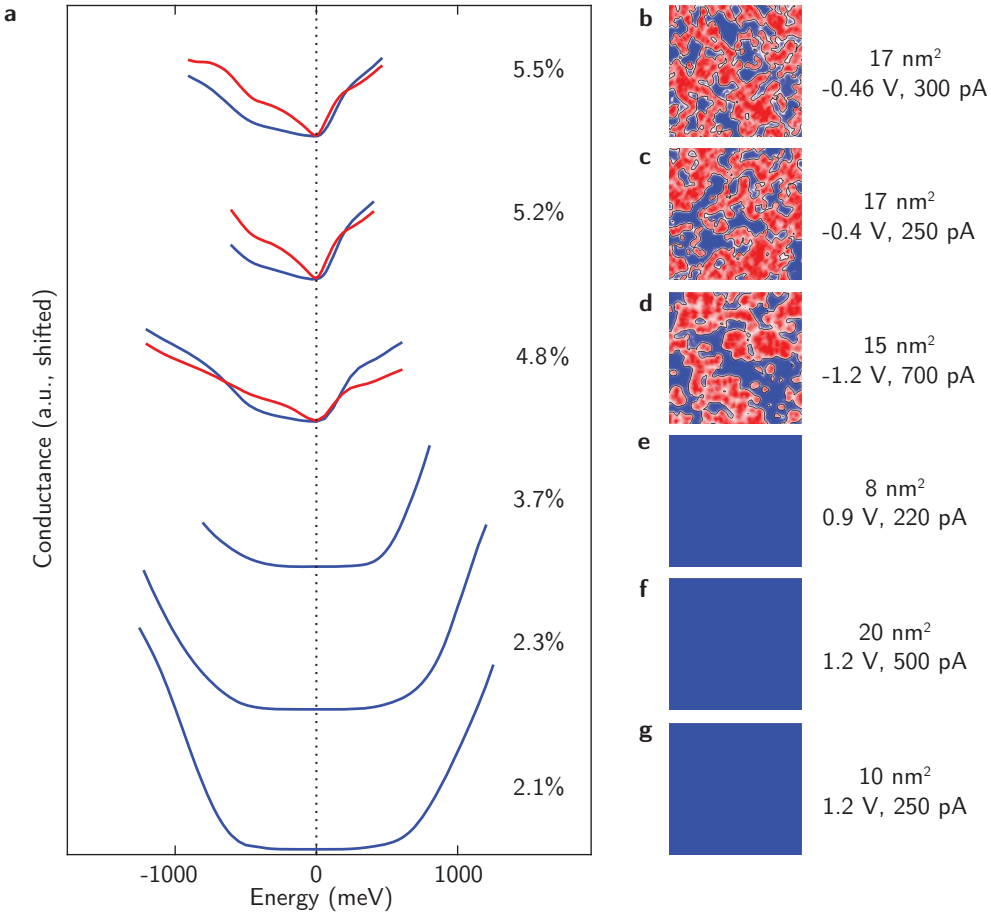

Figure 4.8: Evolution of the electronic structure with increasing dopant atoms concentration. **a**, Density of states spectra at different doping levels, each averaged over regions with Mott gap (blue) and pseudogap (red) as defined by the Mott parameter in **b**-**g**. Due to the different setup conditions for the different measurements, the spectra are normalized by their setup conditions (indicated to the right of each panel), $(\mathrm{d}I/\mathrm{d}V)/(I_\mathrm{s}/V_\mathrm{s})$. **b**-**g**, Respective maps of the Mott parameter, where blue indicates a pure Mott gap, and red indicates a pseudogap puddle.

in-gap states? Why is the chemical potential not shifting towards the upper Hubbard band with electron doping?

We propose that we do not observe in-gap states because the electron-electron correlations that cause the opening of the Mott gap in the impurity band are strong enough to push the resulting subbands outside of the Mott gap itself, as illustrated in Fig. 4.9c.

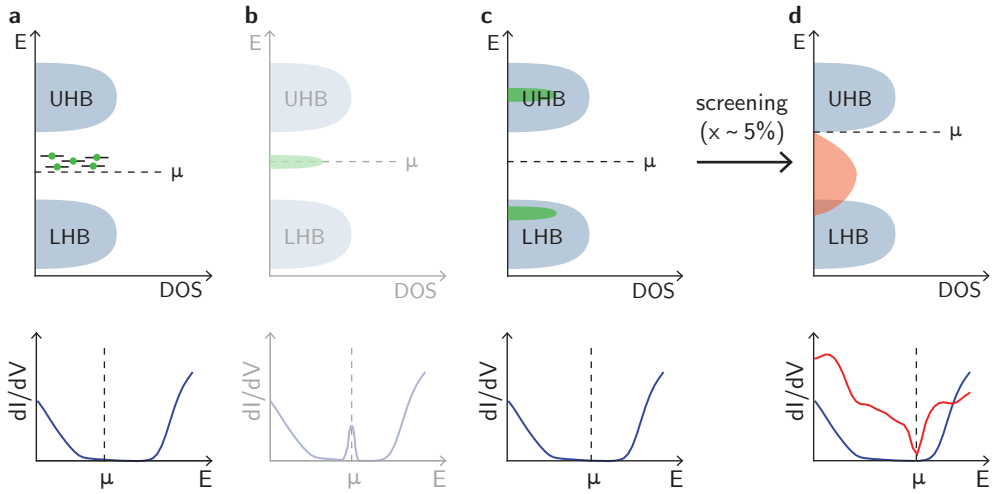

Figure 4.9: Illustration of the melting of the Mott state. **a**, With a very few extra carriers, the dopant energy levels aggregate into a narrow range of energy, however the electrons are still localized on the atomic sites. **b**, The extra carriers would eventually form a band at the Fermi level, with the appearance of in-gap states in the $\mathrm{d}I/\mathrm{d}V$ spectra. This is however not observed in $(Sr_{1-x}La_x)_2IrO_4$. **c**, Mott transition in the impurity band: the impurity band gets split due to the strong Coulomb repulsion, and pushed outside the Mott gap. The chemical potential stays at about mid-gap, at the energy of the impurity band. **d**, At sufficient doping, due to electronic screening, the Mott gap collapses and pseudogap puddles appear.

The fact that the chemical potential stays at about mid-gap upon doping indicates that the dopant electrons are tightly bound to the dopant atom, resulting in very deep dopant electronic states. In other words, the chemical potential is indeed moving to the impurity band, but the latter is located very deep, at about mid-gap. The Mott transition does not influence the position of the chemical potential, that remains roughly corresponding to the binding energy of the extra electrons.

Now that we gave a possible explanation for the low doping regime behavior, let us elucidate how the abrupt collapse to the phase-separated landscape takes place. In a static picture, increasing the dopant concentration would eventually lead to an overlap of the localized wave functions, and to a collapse of the impurity Mott state. However, if we assume the small extension of the wave functions necessary to explain the deep trapping of the extra electrons, the doping threshold for the collapse would have to be much higher than what we measure. We propose that, with increasing doping, screening of the long-range Coulomb interaction by doped carriers leads to an abrupt collapse of the impurity Mott state at doping concentrations lower than one would expect in a static picture.

In the cuprates, similar microscopic processes have initially been proposed, but the Mott state is much more fragile: even weak hole-doping of around 2% can destroy the logarithmic divergence in the resistance [112]. This is due to the much smaller energy scales of the trapping in the cuprates; below the transitions, the material behaves similar to a doped semiconductor, with an impurity band close to the energy of the valence band [112, 113]. This is consistent with the later observation that the dopant centers are quite shallow [101]. Based on our results, we predict that LDA+U calculations on doped iridates will reveal the trapping of La dopant states to be much deeper than the equivalent states in the cuprates.

4.8 Discussion and conclusions

In this chapter, we have presented our SI-STM study of the electronic behavior of Sr_2IrO_4 upon electron doping.

The appearance of a pseudogap at doping $x \approx 5\,\%$ is to date well established by different experimental techniques (STM [92, 94], ARPES [79, 95], optics [76, 96]) and theory [106, 114], with open discussions on the microscopic origin of the pseudogap, as mentioned in Sec. 4.6.2.

At lower doping, instead, the picture is still not confirmed. Due to the strong doping inhomogeneities found by us (Sec. 4.3) and by Ref. [96], it is difficult to study samples in this doping concentration with techniques that average over a big area, such as photoemission, transport and optical spectroscopy. Indeed, ARPES studies in the low-doping regime [79, 80] have contrasting results, both with our STM observations and between each other. However, two optical spectroscopy studies seem to be in partial agreement with our results [76, 96]: Both the studies reveal that in the low doping regime, below $x = 4\,\%$, the strong correlations from the Mott state are still present, with the optical transition corresponding to the Mott gap not shifting in energy, and only partially dampening. Above $x = 5\,\%$ doping, signatures of the pseudogap start to appear in both studies, and the Mott transition peak no longer persists. In Ref. [96], the authors also observe a soft collective mode at 40 meV in the low doping regime. They propose that this soft collective mode stems from the excitation of a frozen correlated state of the electrons pinned by disorder associated with the donor states. This interpretation would be consistent with the frozen Mott state proposed by us.

To conclude this chapter, we would like to go back to the comparison between the electron-doped iridates studied here and hole-doped cuprates. Detailed SI-STM measurements on cuprates, for example, $Ca_{2-x}Na_xCuO_2Cl_2$ and $Bi_2Sr_2CaCu_2O_{8+\delta}$, revealed surprising universalities including the glassy charge order observed in the CuO layer. On first look, $(Sr_{1-x}La_x)_2IrO_4$ seems to be a very different beast: electron

instead of hole doping, Ir instead of Cu, $5d^5$ instead of $3d^9$ electronic configuration. However, our data clearly shows that electronic order and pseudogap are present in $(Sr_{1-x}La_x)_2IrO_4$ as well. Moreover, we believe that the interplay between dopants, pseudogap and order seen here holds for the cuprates too. In general, our results, combined with the bigger picture emerging from literature on doped Sr_2IrO_4, confirm that the phenomenology observed in the low-doping region of the phase diagram of the cuprates is not specific to the copper oxide planes, but generic to a bigger class of two-dimensional lightly doped Mott insulators. By extension, we can expect $(Sr_{1-x}La_x)_2IrO_4$ to become a high-temperature superconductor at only slightly higher doping concentration.